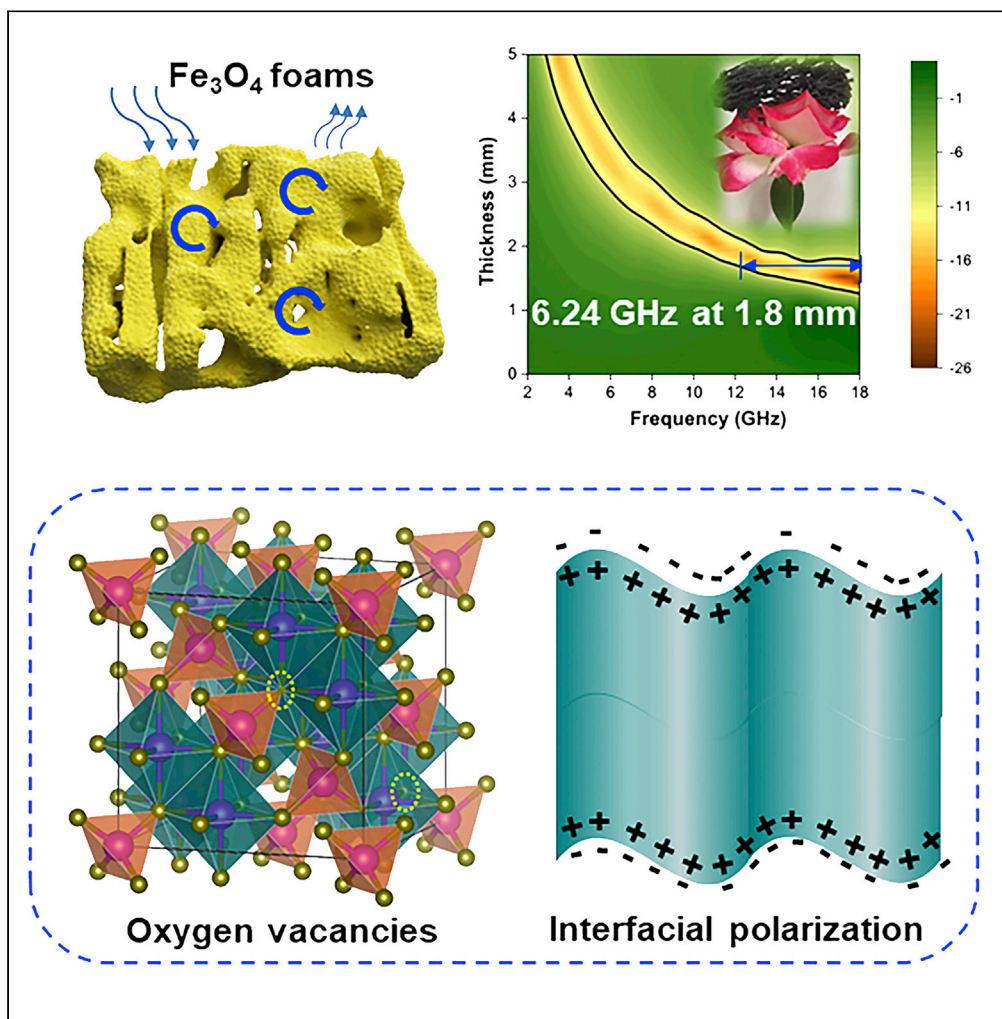


## Article

Microstructure induced dielectric loss in lightweight  $\text{Fe}_3\text{O}_4$  foam for electromagnetic wave absorption

Qing Chang,  
Hongsheng Liang,  
Bin Shi, Hongjing  
Wu

shibinyau@163.com (B.S.)  
wuhongjing@nwpu.edu.cn  
(H.W.)

**Highlights**  
 $\text{Fe}_3\text{O}_4$  foams with 3D structure shaped by folding of 2D curved surface were prepared

Effect of microstructure on conductivity and EMW absorbing property was investigated

Lightweight ( $0.05078 \text{ g/cm}^3$ ) and broad bandwidth absorption (6.24 GHz) were achieved

Chang et al., iScience 25,  
103925  
March 18, 2022 © 2022 The  
Author(s).  
<https://doi.org/10.1016/j.isci.2022.103925>

## Article

# Microstructure induced dielectric loss in lightweight Fe<sub>3</sub>O<sub>4</sub> foam for electromagnetic wave absorption

Qing Chang,<sup>1,2</sup> Hongsheng Liang,<sup>1</sup> Bin Shi,<sup>3,\*</sup> and Hongjing Wu<sup>1,4,\*</sup>

## SUMMARY

**Fe<sub>3</sub>O<sub>4</sub> has been extensively applied in electromagnetic wave absorption field profiting from its advantageous magnetic loss, low cost and environmental benignity. Nevertheless, the inherent drawbacks of high density, low permittivity and easily magnetic aggregation are still the obstacles for pristine Fe<sub>3</sub>O<sub>4</sub> becoming ideal absorbents. To overcome such limitations, a design mentality of constructing 3D structure shaped by curled 2D porous surface is proposed in this study. 3D structure overcomes the easy-agglomeration issue of 2D materials and meanwhile maintains their conductivity. The complex permittivity of samples is regulated by adjusting the microstructure of Fe<sub>3</sub>O<sub>4</sub> to achieve optimum impedance matching. Defect induced polarization and interfacial polarization are the main loss mechanisms. Impressively, the density of S0.5 is only 0.05078 g/cm<sup>3</sup> and the effective absorption bandwidth is up to 6.24 GHz (11.76-18 GHz) at 1.8 mm. This work provided a new insight for structurally improving the EMW absorption performance of pure magnetic materials.**

## INTRODUCTION

Nowadays, the rapid advancement of information technology boosts the wide usage of electronic equipment in military and civil field, and the resultant electromagnetic pollution and interference are increasing seriously and attract more attention (Liu et al., 2021a; Zhang et al., 2021; Zhao et al., 2020a; Wu et al., 2019; Lv et al., 2018). Electromagnetic wave (EMW) absorbents, which can absorb EMW energy and converse into heat energy, have been extensively and deeply researched, and especially, lightweight and broadband EMW absorbents have become research hotspots in recent years to satisfy the stringent requirement (Qin et al., 2021a, 2021b; Zhao et al., 2020b; Wu et al., 2015; Liu et al., 2021b; Li et al., 2021; Zhao et al., 2021).

Magnetite (Fe<sub>3</sub>O<sub>4</sub>), a typical ferrite, has been widely used for EMW absorption owing to its low cost, environmental benignity and advantageous magnetic loss (Wang et al., 2019; Zhou et al., 2020; Wu et al., 2020a). However, single Fe<sub>3</sub>O<sub>4</sub> has not been extensively studied, imputing to the fact that its inherent high density and low permittivity can hardly meet the requirements of advanced absorbers for lightweight and broadband absorption (Tong et al., 2011; Chen et al., 2020; Sun et al., 2011). To achieve high-efficiency absorption, combining magnetic Fe<sub>3</sub>O<sub>4</sub> nanoparticles with dielectric carbon materials is deemed a scheme to reduce the density and broaden the effective absorption bandwidth of absorbents, so various Fe<sub>3</sub>O<sub>4</sub>/C composites represented by Fe<sub>3</sub>O<sub>4</sub>/carbon foams (Meng et al., 2020) and CNT/Fe<sub>3</sub>O<sub>4</sub> aerogels (Jia et al., 2017) emerge in an endless stream in recent years. Unfortunately, these schemes have not addressed the issue for the impedance mismatch and low permittivity from the perspective of Fe<sub>3</sub>O<sub>4</sub> itself, to say nothing of tedious preparation, high cost, and the use of toxic reagents hardly meeting the requirements of industrialization and sustainable development. Accordingly, a handy and low-cost regulation strategy of EMW absorbing performance focusing on Fe<sub>3</sub>O<sub>4</sub> itself is extremely desired.

Constructing porous structure and cavity is another avenue to adjust impedance matching characteristics and tailor electromagnetic parameters of single absorbent (Ma et al., 2021; Yan et al., 2018; Qin et al., 2020a; Yang et al., 2021), because the high porosity can reduce the weight of materials and produce polarization loss at the same time. In the view of structure, porous structures are conducive to the entrance of incident EMW into the absorber so as to ameliorate impedance matching, and moreover, plenty of propagation channels prefer to trap incident EMWs and consume them through multiple reflections (Li et al.,

<sup>1</sup>MOE Key Laboratory of Material Physics and Chemistry Under Extraordinary, School of Physical Science and Technology, Northwestern Polytechnical University, Xi'an 710072, China

<sup>2</sup>College of Chemistry and Chemical Engineering, Shaanxi Key Laboratory of Chemical Reaction Engineering, Yan'an University, Yan'an 716000, China

<sup>3</sup>Center for Translational Medicine Research on Sensory-Motor Diseases, Yan'an University, Yan'an 716000, China

<sup>4</sup>Lead contact

\*Correspondence:  
shibinyau@163.com (B.S.),  
wuhongjing@nwpu.edu.cn  
(H.W.)

<https://doi.org/10.1016/j.isci.2022.103925>



2019a; Liang et al., 2021). Consequently, a few efforts have been devoted to fabricate spherical porous Fe<sub>3</sub>O<sub>4</sub> absorbents. For example, multilevel nanoporous Fe<sub>3</sub>O<sub>4</sub> microspheres prepared by Qing et al. (2014) display dual absorptions at both low frequencies and high frequencies. Li's group (Li et al., 2016) prepared Fe<sub>3</sub>O<sub>4</sub> hollow/porous spherical chains also display outstanding absorption capability (~52.8 dB at 2.6 mm). However, the limited improvement of complex permittivity is still a stumbling block for pure Fe<sub>3</sub>O<sub>4</sub> to achieve satisfactory EMW absorbing performance, let alone practical application.

Two-dimensional (2D) structure brings down for the improvement of complex permittivity, owing to its features of small thickness and high specific surface area, in which the former improves conductivity loss by shortening conductive paths and the latter generate enhanced polarization loss through abundant interfaces (Qin et al., 2020b; Sun et al., 2017; Han et al., 2017). For example, Che's group (Li et al., 2019b) reported that the imaginary part of permittivity could be enhanced by the collective migration of polarization electrons near the interfacial planes of ZnCo<sub>2</sub>O<sub>4</sub> flakes so as to improve the EMW absorption ability. Liu et al. (2018) referred to that sheet-shaped particles would exhibit increased permittivity for the enhancement of interface polarization caused by the large specific surface. However, agglomeration interaction between 2D nanostructures will seriously affect their dissipation capacity for EMW, particularly serious for magnetic particles. Based on the issues above, building a spatial three-dimensional (3D) structure constructed by curled 2D surface may be a perfect solution to overcome agglomeration while maintaining the conductivity of 2D materials. Coupled with porous architecture, the unique shape can reduce density, improve the impedance matching, and further promote the dielectric loss at the same time.

Here, Fe<sub>3</sub>O<sub>4</sub> foams with unique 3D structure shaped by the folding of 2D curved surface were prepared using a facile sol-gel autocombustion method. The violent release of heat and gas during combustion process facilitated the formation of Fe<sub>3</sub>O<sub>4</sub> porous foam, the density of which is even low to 0.03368 g/cm<sup>2</sup> and the specific surface area is as high as 61.64 m<sup>2</sup>/g. The complex permittivity of Fe<sub>3</sub>O<sub>4</sub> porous foam is regulated by adjusting the microstructure of Fe<sub>3</sub>O<sub>4</sub> foams to achieve optimum impedance matching, which is the prerequisite of excellent absorption performance. The defect induced polarization, which caused by oxygen vacancies and lattice defects, together with interfacial polarization are the main loss mechanisms. Impressively, the EAB of S0.5 is as wide as 6.24 GHz at a small thickness of 1.8 mm, which outperforms all reported pure Fe<sub>3</sub>O<sub>4</sub> absorbents (Tong et al., 2014; Han et al., 2014) and even surpasses most Fe<sub>3</sub>O<sub>4</sub>-based composites (Zhang et al., 2018; Qiao et al., 2018; Zhou et al., 2019; Liu et al., 2020; Gao et al., 2020; Jin et al., 2021). Moreover, the qualified bandwidth (90% absorption) achieves 15.52 GHz (2.48-18 GHz) under 1.2-5.0 mm thicknesses. Our work provided a new insight for improving the EMW absorption performance of pure magnetic materials by structure adjustment.

## RESULTS AND DISCUSSION

Figure 1A graphically depicts the preparation process of Fe<sub>3</sub>O<sub>4</sub> foams through a sol-gel autocombustion method. Briefly, Fe<sup>3+</sup> chelated with citric acid (CA) at a condition of pH = 7 to obtain sol solutions of ferric citrate firstly. After drying, xerogels constructed by network-like ferric citrate were harvested. When the xerogels were ignited, a large amount of gas (H<sub>2</sub>O, CO<sub>2</sub>, CO, NO, NO<sub>2</sub>, H<sub>2</sub>, CH<sub>4</sub>) released during the combustion process endowed the products fluffy structures, simultaneously reduced part of Fe<sup>3+</sup> to Fe<sup>2+</sup> and eventually produced lightweight Fe<sub>3</sub>O<sub>4</sub> foams. As evidence, the prepared Fe<sub>3</sub>O<sub>4</sub> foam can be placed on a rose flower easily without obvious deformation in the petals (Figure 1A). As reported, the maximum temperature of combustion reaction is related to the stoichiometric ratio of fuel (CA) and oxidant (nitrate). Specifically, the temperature of rich-fuel system is higher, while the temperature of lean-fuel system is lower, even incomplete combustion (Hua et al., 2012). As shown in Figure 1B, when increasing the ratio of citric acid from 0.3 to 0.9, the surface of microstructure gradually become smooth and the thickness get thinner. What's more, the open channels throughout the structure gradually decrease, and are replaced by massive caves formed by folded of curved surface. This is derived from the fact that the increased proportion of CA promotes the release of heat and gas, so as to promote crystal fusion and volume expansion of products (Zhang et al., 2016), which produce smoother surfaces, thinner thickness and more folds, and further reduce the density and increase the specific surface area of products, which may enhance the polarization loss. Briefly speaking, the morphology and electromagnetic parameters of the products can be modulated by simply changing the adding amount of CA.

The crystal phases and compositions of synthesized products were characterized by XRD. When the ratio of CA changes in the range of 0.3-0.9, the as-obtained samples are all cubic spinel Fe<sub>3</sub>O<sub>4</sub> (JCPDS card No.

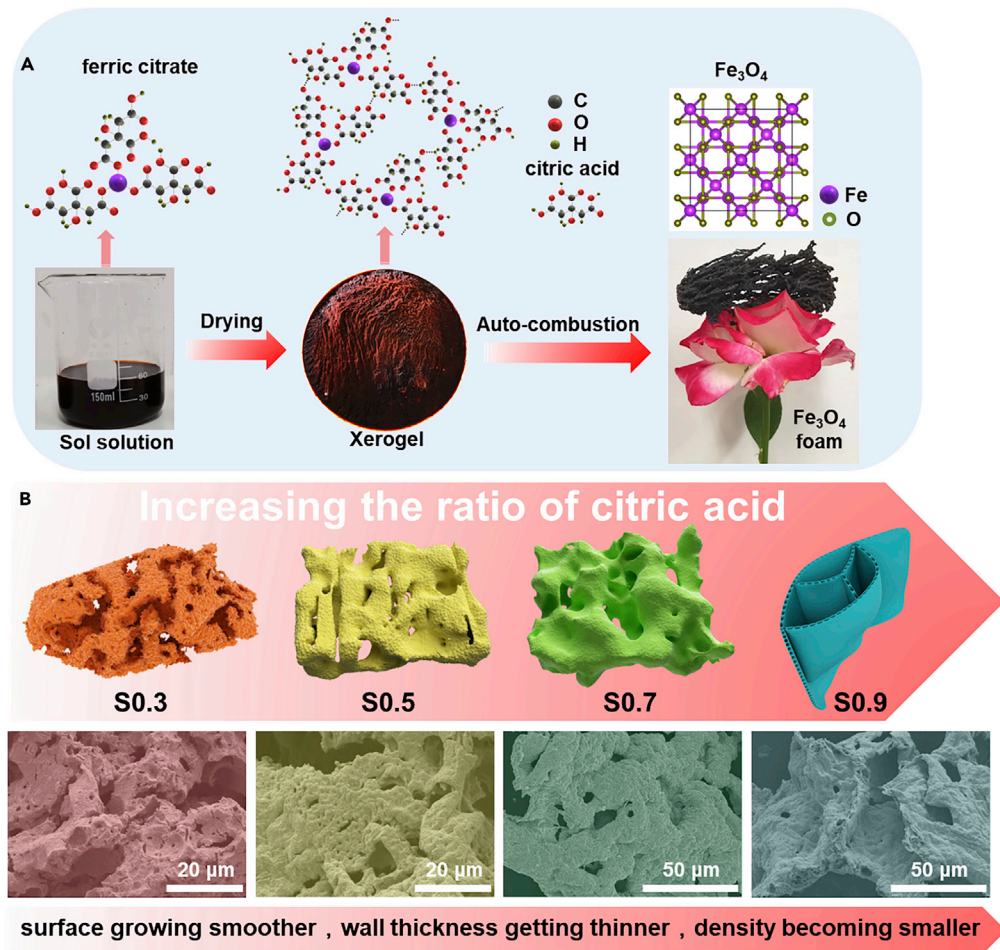


**Figure 1. Synthesis scheme and morphology characterization of  $\text{Fe}_3\text{O}_4$  foams**

Synthesis scheme (A) of  $\text{Fe}_3\text{O}_4$  foams using sol-gel autocombustion method and the morphological characteristics (B) of  $\text{Fe}_3\text{O}_4$  foams under different ratio of citric acid.

65-3107) with high purity (Figure 2A), while the product of S0.1 is  $\text{Fe}_2\text{O}_3$  (Figures S1 and S2), indicating that only when the fuel ratio changes within an appropriate range, can the  $\text{Fe}_3\text{O}_4$  foam be successfully obtained. Meanwhile, the sharp peaks in Figure 2A hint the high crystallinity of  $\text{Fe}_3\text{O}_4$ , proving that the heat released in autocombustion process at ignition temperature of 200°C is enough to obtain  $\text{Fe}_3\text{O}_4$  with high crystallinity. The crystal structure in Figure 2B well exhibits the typical  $Fd\bar{3}m$  space group of  $\text{Fe}_3\text{O}_4$ , in which  $\text{Fe}^{3+}$  mostly on octahedral sites (green) and  $\text{Fe}^{2+}$  mostly on tetrahedral sites (orange). The Raman spectra further confirm the crystal type of products (Figure 2C), in which the peaks at 219, 284 and 397  $\text{cm}^{-1}$  are assigned to  $E_{2g}$ ,  $T_{2g}$  and  $A_{1g}$  model of cubic spinel  $\text{Fe}_3\text{O}_4$  (Xu et al., 2019). Noteworthily, a distinct redshift occurs in the peaks of S0.7 and S0.9 in comparison with the other samples, meaning the increase of residual stress and lattice distortion (Chang et al., 2021a). As is reported, lattice defects will cause the uneven distribution of local charge and result in polarization loss of EMW (Qin et al., 2021b; Liang et al., 2020). Therefore, it is preliminarily speculated that S0.7 and S0.9 may produce stronger lattice defect polarization than S0.3 and S0.5.

The surface element valences and chemical bond types of the  $\text{Fe}_3\text{O}_4$  foams are further investigated by XPS. The full spectra (Figure 2D) prove the presence of Fe, O and C elements in all samples. Taking S0.5 as an example, the enlarged drawings of the part in red dotted frame are shown in Figures 2E and 2F, respectively. In detail, the two major peaks at 710 and 725 eV in the high-resolution  $\text{Fe}2\text{p}$  XPS spectrum (Figure 2E) correspond to  $\text{Fe}2\text{p}_{3/2}$  and  $\text{Fe}2\text{p}_{1/2}$ , respectively (Shi et al., 2019; He et al., 2020), and peak fitting further reveal the coexistence of  $\text{Fe}^{3+}$  and  $\text{Fe}^{2+}$ . Meanwhile, a distinct O1s peak in full spectrum prove the high content of oxygen element, which was further divided into Fe-O bonds (O1), oxygen vacancy (O2) and O-H bonds (O3).

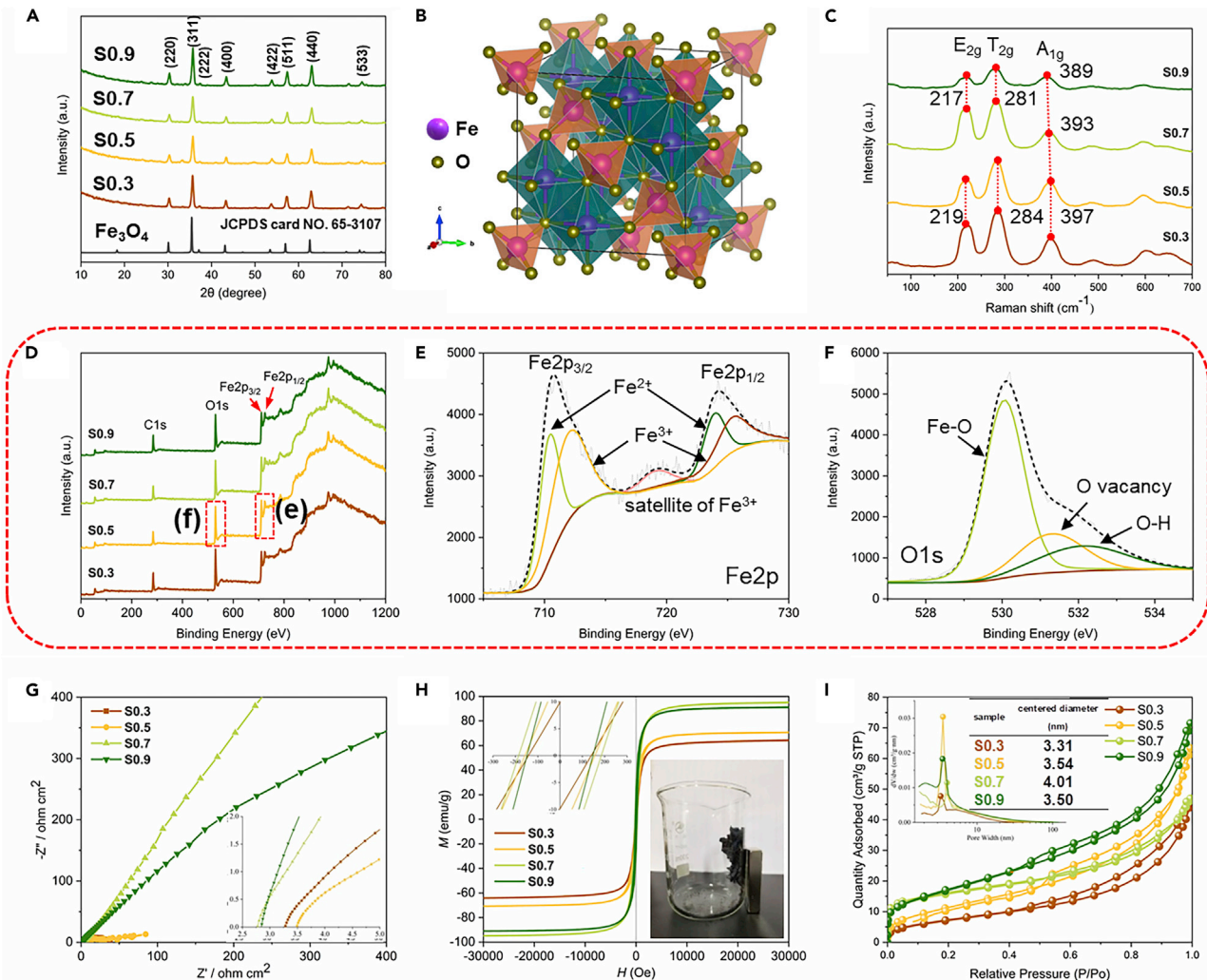


**Figure 2. XRD patterns**

(A–I) (A), crystal structure (B) and Raman spectra (C) of the  $\text{Fe}_3\text{O}_4$  foams; full-scan XPS spectra (D) and high-resolution Fe2p (E) and O1s (F) spectra of S0.5; Nyquist curves (G), hysteresis loops (H) and  $N_2$  absorption-desorption isotherms (I) of as-obtained  $\text{Fe}_3\text{O}_4$  foams.

(Figure 2F). The high-resolution spectra of Fe2p, O1s, and C1s for S0.3, S0.5 and S0.9 were displayed in Figure S3. It is worth noting that the concentration of active vacancy oxygen, namely oxygen defect, is proportional to the ratio of O2 to O1. In terms of our samples, the concentrations of oxygen defects in the four samples are similar, which are in the range of 0.2022–0.2252 (Table S1), expressing that the oxygen defect polarization in  $\text{Fe}_3\text{O}_4$  foams are equivalent. In addition, the small peak of C1s (Figures 2D and S3) may originate from the little residual carbon left after the combustion of Fe (iii)-oxalate complexes.

The conductivity and magnetic properties were measured through EIS and magnetic measurement system, respectively. The Nyquist curves are shown in Figure 2G, it is worth to note that the Nyquist curves of S0.3 and S0.5 are composed of a semicircle part in high frequency, representing charge-transfer resistance ( $R_{\text{ct}}$ ) namely impedance of material, and straight line part in low frequency (Fang et al., 2020). According to the curve fitting results, the  $R_{\text{ct}}$  of S0.3 and S0.5 are 13.86 ohm/cm<sup>2</sup> and 4.38 ohm/cm<sup>2</sup> orderly, impressing a better conductivity of S0.5 than S0.3. On the contrary, the Nyquist curves of S0.7 and S0.9 are almost straight line in the whole test frequency, implying the high conductivity of S0.7 and S0.9. The EIS results demonstrate that with the increase of CA, the conductivity of  $\text{Fe}_3\text{O}_4$  foams increases gradually, especially when the ratio of CA is above 0.5, the conductivity is greatly improved, signifying strong conduction loss capability of S0.7 and S0.9. The lurking reasons is speculated that the burst of heat in a fuel rich system

promotes the crystal melting and crystallinity of  $\text{Fe}_3\text{O}_4$ , which reduce the energy barrier of electron transfer between  $\text{Fe}^{2+}$  and  $\text{Fe}^{3+}$ , so as to raise the conductivity of samples (Huang et al., 2011). The hysteresis loops in Figure 2H prove the ferromagnetism characteristic of products and the detailed data are listed in Table S2. The  $M_s$  values of S0.3 (64.39 emu/g) and S0.5 (70.85 emu/g) in room temperature are much lower than those of bulk  $\text{Fe}_3\text{O}_4$  (92 emu/g) (Qing et al., 2014). Generally speaking,  $M_s$  values for magnetic nanomaterials are lower than those for corresponding bulk materials, owing to the fact that the increasing spin disorder on the surface induced by the decreased grain size of magnetic nanomaterials would significantly reduce the total magnetic moment (Jia et al., 2017; Jiang et al., 2017; Ma et al., 2021; Tong et al., 2015). However, it is unexpected that the  $M_s$  values of S0.7 (95.17 emu/g) and S0.9 (91.25 emu/g) are very close to that of bulk  $\text{Fe}_3\text{O}_4$ , which may attribute to the large crystal sizes and high crystallinity of the as-obtained samples. This result confirmed the previous speculation that the large amount of heat generated in the rich-fuel system improves the crystallinity of products. Surprisingly, the  $H_c$  values of as-obtained  $\text{Fe}_3\text{O}_4$  foams (Table S2) enhance almost two orders of magnitude than bulk  $\text{Fe}_3\text{O}_4$  (1.88 Oe). It is widely known that the larger  $H_c$  of the absorbents suggests a stronger magnetic anisotropy and will result in stronger natural magnetic resonance at a high frequency (Han et al., 2014). Under the action of a magnet, the sample is in suspension (illustrated photo in Figure 2H), vividly displaying the lightweight and strong magnetic characteristics of the as-prepared  $\text{Fe}_3\text{O}_4$  foams.

The permanent porosity of as-gained  $\text{Fe}_3\text{O}_4$  foams was evaluated through  $\text{N}_2$  absorption-desorption isotherms. As shown in Figure 2I, typical type-IV isotherms with apparent type-H3 hysteresis loops imply the mesoporous characteristics of the  $\text{Fe}_3\text{O}_4$  foams, and the shape of type-H3 hysteresis loops is related to the formation of slit-like pores in the aggregates of plate-like particles (Qin et al., 2020b; Sun et al., 2017). In addition, the pore size distribution curves (insert in Figure 2I) further confirm that the four samples have similar mesoporous structure, the center diameter of which are in the ranges of 3.31–4.01 nm. Likewise, the specific surface area of  $\text{Fe}_3\text{O}_4$  foams rise from 26.74, 42.88, 57.68 to 61.64  $\text{m}^2/\text{g}$ , accompanying by the increased content of CA (Table S2 and Figure S4), which is much higher than that of porous magnetite spheres (24.3  $\text{m}^2/\text{g}$ ) (Huang et al., 2011) and hollow magnetite microspheres (12.3  $\text{m}^2/\text{g}$ ) (Xiong et al., 2012). It has been widely accepted that increased specific surface area of absorbent is benefit to enhance interfacial polarization stemming from heterogeneous interfaces of absorbers and adhesive such as paraffin wax. Therefore, it can be inferred that from S0.3 to S0.9, the interfacial polarization gradually enhances. Impressively, the density of  $\text{Fe}_3\text{O}_4$  foams declines sharply from 0.2695, 0.05078, 0.04673 to 0.03368  $\text{g}/\text{cm}^3$ , benefiting from the violent release of gas (Table S2). These data verify the previous discussion on Figure 1 that the increased CA releases more heat energy and gas during combustion, so as to improves the specific surface area and reduce the density of the samples at the same time.

SEM and TEM were carried out to further investigate the microstructure and pore characteristics of  $\text{Fe}_3\text{O}_4$  foams. S0.3 displays rough block structures with many open channels and deep cracks (Figures 3A, 3B, and S5A–S5F) and the wall thickness of block is about 9.14  $\mu\text{m}$ . The high-resolution SEM image (Figure 3C) show clearly that the rough wall is constructed by compactly arranged  $\text{Fe}_3\text{O}_4$  particles in the sizes of 0.2–1.0  $\mu\text{m}$ . Increasing the ratio to 0.5, the morphology changed to distinctive 3D hollow porous structures, which shaped by the folding of curved surface (Figures 3D and S6A–S6D). The thickness of curved surface is 0.74–0.78  $\mu\text{m}$  with numerous shallow cavities (Figures 3E and S6F). The relatively smooth surface is composed by the mutual cementation of  $\text{Fe}_3\text{O}_4$  particles, and the holes formed by surface convolution are clearly visible (Figures 3F and S6E). As expected, the raised ratio of fuel promotes the release of heat and gas during autocombustion, leading to the cementation of  $\text{Fe}_3\text{O}_4$  particles and formation of initial nanopores in wall. The EDS mapping (Figure 3M) demonstrates that Fe and O element distribute evenly in the whole microstructure with no observation of C element, expressing that the content of residual carbon is negligible after high temperature combustion. Continue to increase the proportion to 0.7, the surfaces of 3D structures become much smoother with sparse holes (Figures 3G and S7A–S7D). The holes at a corner of folded surfaces show clearly the wall become thinner, which is between 0.60 and 0.67  $\mu\text{m}$  (Figure 3H). The partial enlarged view of show that the flat and smooth surface is composed of countless bonded  $\text{Fe}_3\text{O}_4$  nanoparticles (Figures 3I and S7E), which may be due to the fact that the boosted heat during burning promote the fusion of nanoparticles so as to make the surface more complete and smoother. S0.9 displays nearly smooth surface with wall thickness of 0.40–0.50  $\mu\text{m}$  without obvious graininess (Figures 3J–3L and S8A–S8D). Noteworthily, the interlayer of walls is full of various penetrating holes, which reduced the mass and improved the specific surface area of samples greatly, confirming the results of BET test. Additionally, the numerous pores are beneficial to multiple reflection of EMW. It is noteworthy that the residual

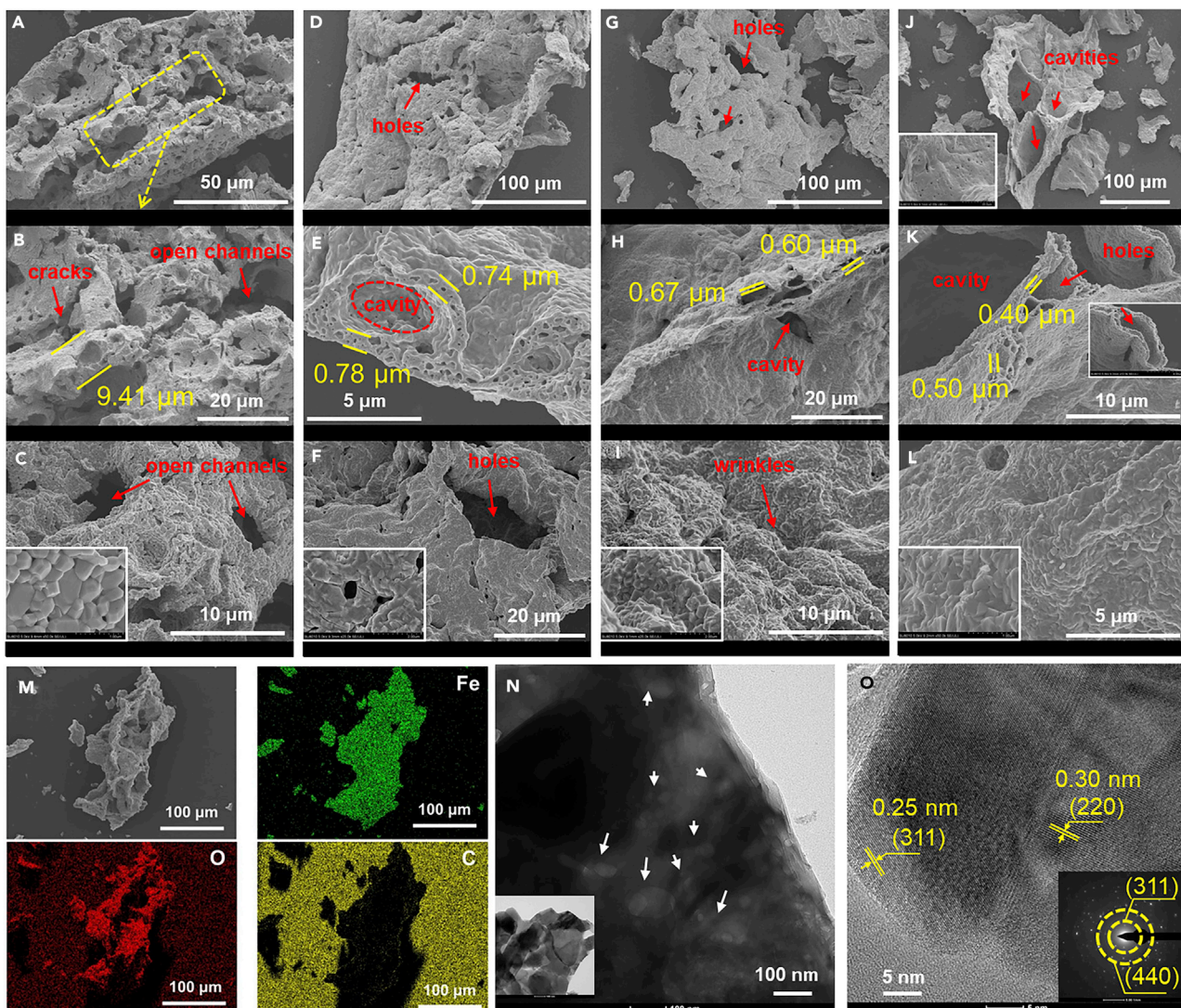


**Figure 3. SEM images of S0.3**

(A–O) (A–C), S0.5 (D–F), S0.7 (G–I), S0.9 (J–L); mapping of S0.5 (M); TEM images (N) and selected area electron diffraction (O) of S0.5.

carbon is negligible in all samples (Figures 3M, S5C, S7F, and S8H), which indicates that the dipole polarization produced by carbon-containing functional groups is insignificant. To gain further insight, the details of microstructure and crystal lattice are investigated deeply through TEM. Taking S0.5 as an example, these 3D microstructures are formed by stacked planar  $\text{Fe}_3\text{O}_4$  without obvious granular structures (inset in Figure 3N), demonstrating that  $\text{Fe}_3\text{O}_4$  grains have been integrated to form a planar structure, which is convenient for the electron transfer between  $\text{Fe}^{3+}$  and  $\text{Fe}^{2+}$  (Lv et al., 2014). Moreover, the partial enlarged view intuitively exhibited the porous characteristics of planar  $\text{Fe}_3\text{O}_4$  (Figure 3N). The lattice fringes with spacing of 0.25 and 0.30 nm in the high-resolution images (Figure 3O) correspond to the lattice plane of (311) and (200) respectively, confirming the existence of spinel  $\text{Fe}_3\text{O}_4$  again. Moreover, the selected area electron diffraction (SAED) of the sample also displays typical crystal plane spacing of  $\text{Fe}_3\text{O}_4$  (inset in Figure 3O).

To clarify the relationship between microstructures of  $\text{Fe}_3\text{O}_4$  foams and their electromagnetic behavior, the complex permittivity ( $\epsilon_r = \epsilon' - j\epsilon''$ ) and permeability ( $\mu_r = \mu' - j\mu''$ ) are investigated (Figure S9), in which the real parts ( $\epsilon'$  and  $\mu'$ ) and imaginary parts ( $\epsilon''$  and  $\mu''$ ) represent the storage and dissipation of electric and magnetic energy, respectively. Significantly, both the  $\epsilon'$  and  $\epsilon''$  values of the obtained  $\text{Fe}_3\text{O}_4$  foams are higher than that of bulky  $\text{Fe}_3\text{O}_4$  ( $\epsilon' 4.6\text{--}5.2$ ,  $\epsilon'' 0.1\text{--}1.5$ ) (Deng et al., 2020), illustrating that the 3D foam structure greatly improve

the dielectric properties of pure Fe<sub>3</sub>O<sub>4</sub>. Overall, accompanying the increased frequency, the  $\epsilon'$  values of all samples show a downward trend with some small fluctuations, demonstrating a typical frequency dispersion behavior. In terms of  $\epsilon''$ , S0.7 and S0.9 have higher  $\epsilon''$  values (5-12) in the whole frequency range, which may benefit from the smooth and seamless surface constructed by molten Fe<sub>3</sub>O<sub>4</sub> nanoparticles. According to free electron theory ( $\epsilon'' = 1/2\epsilon_0\pi\rho f$ ), where  $\epsilon_0$  is the permittivity in vacuum,  $\rho$  is the resistivity and  $f$  is the EMW frequency, high  $\epsilon''$  values originate from high conductivity, which is consistent with the inference of EIS, and are conducive to producing strong conduction loss (Cui et al., 2019; Jin et al., 2020). However, it must be pointed that eddy current induced by high conductivity under the action of EMW will in turn lead to the strong reflection of EMW, which is unfavorable to impedance matching. In addition, the three small resonance peaks at 7 GHz, 10 GHz and 13 GHz are ascribed to the polarization relaxation induced by lattice defects and oxygen defects referred to in Raman and XPS analysis. Comparatively, S0.3 and S0.5 displayed relatively moderate  $\epsilon''$  values (around 5) except for the two high peaks at 13.20 GHz (14.88) and 15.44 GHz (10.32) respectively. Commonly, proper  $\epsilon''$  value is benefit for impedance matching, which is convenient for the entrance of EMW. Moreover, the strong resonance peak in S0.3 mainly induced by the oxygen defects polarization corroborating the XPS results. Ultimately, the dielectric loss factor ( $\tan \delta_e$ ) reveals that S0.7 and S0.9 own higher dielectric loss in the whole frequency range, which is dominated by stronger defect polarization (lattice defects and oxygen vacancies) and interfacial polarization originating from large specific surface area. As for S0.3 and S0.5, the dielectric loss is slightly weaker in 2-12 GHz, and then increase greatly when the frequency is above 12 GHz. Specifically, the dielectric loss of S0.3 mainly comes from oxygen defect polarization, while for S0.5, the dielectric loss ability is determined by oxygen defect polarization and interfacial polarization originating from increased specific surface area jointly.

Moreover, the  $\mu_r \sim f$  curves of the four samples are shown in Figures S9D and S9E. Notably, the energy transfer from permeability to permittivity was observed in the four samples (Zhang et al., 2015), which is consistent with the aforementioned high conductivity. Obviously, the enhanced conductivity leads to increased  $\epsilon$  and decreased  $\mu$ . Especially, the  $\mu'$  values are less than one in medium and high frequency, and even negative  $\mu''$  values appears in the range of 9-18 GHz (Figure S9E). This phenomenon can be explained by the fact that eddy current can be easily formed in the high conductive materials under the action of alternating electromagnetic field, which conversely induce new magnetic field. Once the conductivity of material approaches the percolation threshold, the resultant eddy current will shield the penetration of EMW and radiate the magnetic energy out of absorber, reducing its permeability and producing eddy current loss (Zhang et al., 2020; Guo et al., 2015; Yang et al., 2022). Additionally, the small fluctuation at about 4.5 GHz originates from natural resonance, which verified by the distinct resonance peak at the same frequency in  $\tan \mu \sim f$  curves (Figure S9F). As is well known, if eddy current loss is the leading factor of magnetic loss, the  $C_0$  values will remain constant with the varied frequency (Wu et al., 2020). As shown in Figure S10E, the  $C_0$  values of S0.7 and S0.9 keep unchanged in the frequency of 10-18 GHz, proving the existence of eddy current loss. Nevertheless, the  $C_0$  values of all samples decrease slowly in the frequency of 2-10 GHz, implying the existence of natural resonance and exchange resonance. Considering the resonance peaks occur in the low frequency region of  $\mu'' \sim f$  curves, we confirm the existence of natural resonance, which originates from the ferromagnetic nature of Fe<sub>3</sub>O<sub>4</sub>.

Debye relaxation is investigated to further explore the source of dielectric loss. According to Debye relaxation theory (Wu et al., 2020b), the relationship between  $\epsilon''$  and  $\epsilon'$  can be expressed as following:

$$\left(\epsilon' - \frac{\epsilon_s + \epsilon_\infty}{2}\right)^2 + (\epsilon'')^2 = \left(\frac{\epsilon_s - \epsilon_\infty}{2}\right)^2 \quad (\text{Equation 1})$$

where  $\tau$  stands for polarization relaxation time,  $\epsilon_s$  for static permittivity, and  $\epsilon_\infty$  points to the high-frequency limited permittivity. A Cole-Cole semicircle corresponds to a Debye relaxation process. As shown in Figure S10A, S0.3 has the most Cole-Cole semicircles, which echo to the intense resonance peak at 13.20 GHz in the  $\epsilon'' \sim f$  curve, proving the dominance of oxygen defect polarization in S0.3 again. Similarly, three Cole-Cole semicircles originating from oxygen defect polarization also exist in S0.5 (Figure S10B). Additionally, a distinct tailing observed confirms the enhanced conductivity. Comparatively, two irregular semicircles followed by a long tailing existing in S0.7 and S0.9, proving the coexistence of defect polarization coming from oxygen vacancies and lattice defects, and conduction loss (Wei et al., 2022). What's more, the severely deformed Cole-Cole semicircles reveal the enhanced interfacial polarization owing to the significantly increased specific surface area. The change in dielectric loss mechanism of the Fe<sub>3</sub>O<sub>4</sub> foams varied the ratio of CA can be explained as follows: when the fuel is insufficient (S0.3), the rough surfaces scattered with cracks, which result from the less released heat and gas, have a small specific surface

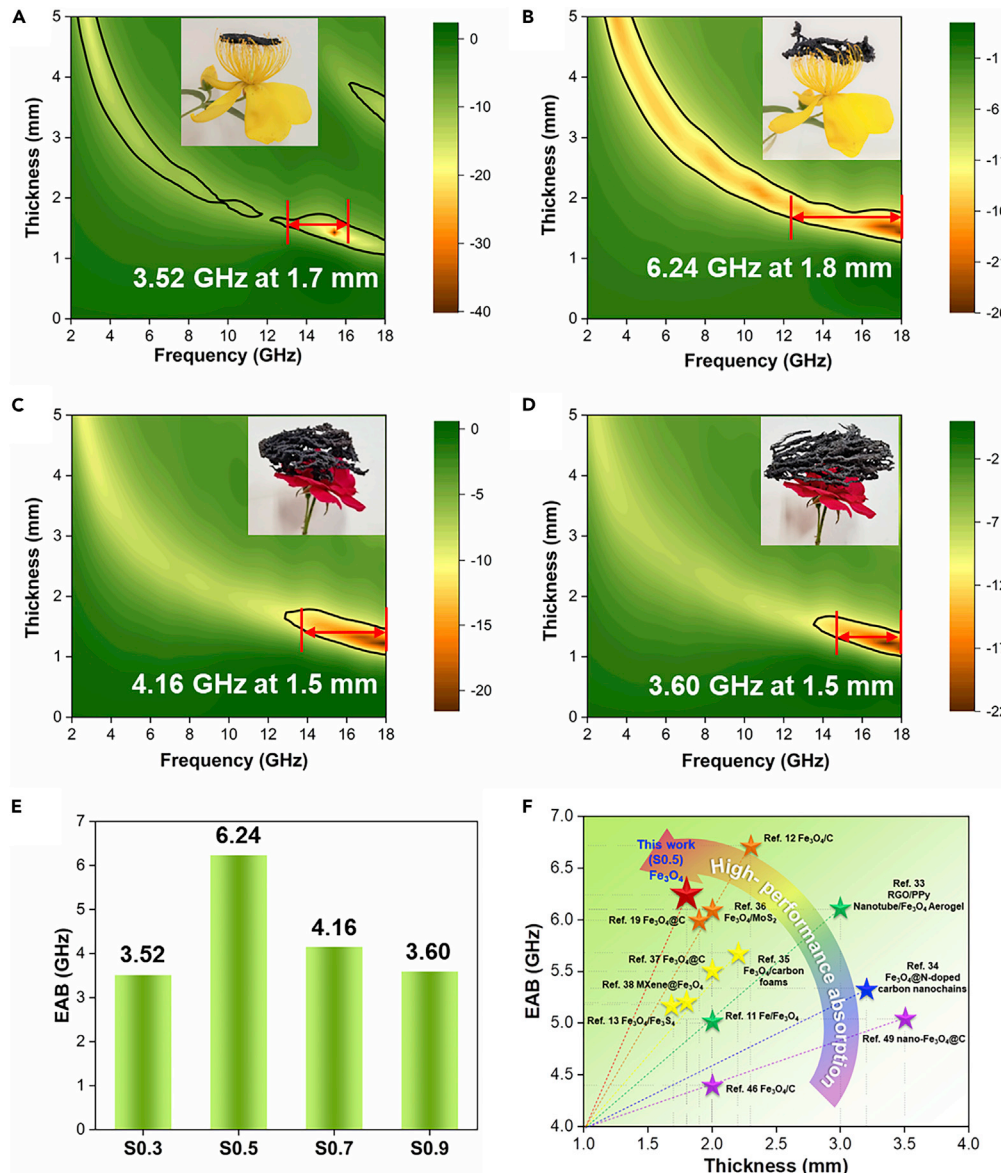


**Figure 4. 2D plots showing the frequency dependence of RL for S0.3**

(A-D) S0.3 (A), S0.5 (B), S0.7 (C) and S0.9 (D).

(E) the inserts are the photos of lightweight Fe<sub>3</sub>O<sub>4</sub> samples placed on the stamens of *Hypericum longistylum* Oliv and petals of Chinese rose; comparison of EAB for the as-obtained Fe<sub>3</sub>O<sub>4</sub> foams.

(F) EMW absorption performance of S0.5 and Fe<sub>3</sub>O<sub>4</sub>-based absorbing materials reported in literature.

area and thereby produce weak interfacial polarization. Therefore, defects polarization induced by oxygen vacancies becomes the dominant loss mechanism in S0.3. Along with the increased fuel ratio, the violent release of heat and gas makes the product fluffy, which greatly improve the specific surface area of samples, and facilitates the melting of Fe<sub>3</sub>O<sub>4</sub> nanoparticles, which make the product surface smoother and reduce the energy barrier of electron exchange between Fe<sup>2+</sup> and Fe<sup>3+</sup> simultaneously (Xiong et al., 2012), so as to rise the interfacial polarization and conductivity greatly. Moreover, the defect polarization derived from lattice defects and oxygen vacancies is also enhanced tremendously with the increased CA. Briefly, the dielectric loss of Fe<sub>3</sub>O<sub>4</sub> foams can be adjusted effectively simply by controlling the ratio of CA.

EMW absorption performances of the four samples are shown in Figures 4A–4D. Reflection loss (RL) is commonly applied to evaluate the EMW absorption property of absorber. When more than 90% of the

incident EMW is absorbed, the value of  $RL$  is less than  $-10$  dB, namely efficient absorption, and the corresponding widest frequency range is efficient absorption bandwidth (EAB). There is no doubt that S0.5 displays the optimal EMW absorption performance. The EAB reaches  $6.24$  GHz ( $11.76$ – $18$  GHz) at a small thickness of  $1.8$  mm, achieving the widest EAB among the reported single  $\text{Fe}_3\text{O}_4$  absorbent so far and even beyond most of the  $\text{Fe}_3\text{O}_4$ -based composites (Zhang et al., 2018; Qiao et al., 2018; Zhou et al., 2019; Liu et al., 2020; Gao et al., 2020; Jin et al., 2021). The qualified bandwidth is up to  $15.52$  GHz ( $2.48$ – $18$  GHz) by changing the thickness from  $1.2$  to  $5.0$  mm. Similarly, the EMW absorption performance of S0.3 also meets the basically requirement relying on its qualified absorption bandwidth almost covering  $2$ – $18$  GHz. However, the poor EAB of  $3.52$  GHz seriously limits its practical application. As for S0.7 and S0.9, the valid absorption band locates in high-frequency region of  $13$ – $18$  GHz and the EAB is  $4.16$  and  $3.60$  GHz at a small thickness of  $1.5$  mm, respectively, which have little practical application value. The inserts in Figures 4A–4D show that the as-obtained  $\text{Fe}_3\text{O}_4$  foams can be placed on the stamens and petals of flowers without obvious deformation, highlighting their lightweight characteristics. In addition, the volume of samples becomes larger and larger with the increasing of CA, which provides macroscopic proof for the deduction of SEM Figure 4E intuitively present the EAB of the four samples, and the superior performance of S0.5 is self-evident. Even if compared with existing  $\text{Fe}_3\text{O}_4$ -based composites in literature, our  $\text{Fe}_3\text{O}_4$  foam (S0.5) still exhibits prominent EMW absorbing performance (Figure 4F).

To better understand the EMW absorption mechanisms, impedance matching characteristic and EMW attenuation property of the materials are investigated. As is known to all, impedance matching and attenuation capability are two key factors that determine the performance of EMW absorption, in which the former is a prerequisite determining whether the incident EMW can enter absorbers, and the latter is the ability of absorbers consuming incident EMW.

The delta-function method was applied to evaluate the impedance matching degree between our materials and free space (Chang et al., 2021b), and the relative formulas are listed in Equations 1–3 in supplemental information. The delta value maps of  $\text{Fe}_3\text{O}_4$  foams are presented in Figure S11, in which the larger the green zone ( $|\Delta| \leq 0.4$ ) is, the better impedance matching of the absorbent is. Intuitively, the order of impedance matching is: S0.5>S0.3>S0.7>S0.9. The impedance matching characteristic of absorbents is influenced by composition and structure. As far as our samples are concerned, they are all pure  $\text{Fe}_3\text{O}_4$ , and thus the effect of components is excluded. Therefore, structure characteristic becomes the main factor affecting impedance matching. When the ratio of CA rise from  $0.3$  to  $0.5$ , the complex permittivity is properly improved along with the replacement of rough blocky structure by smooth curved surfaces, which is helpful to improve the impedance matching. With the ratio further improved to  $0.7$  and above, the eddy current induced by excessive conductivity will prevent EMW from entering the absorbents, namely deteriorating impedance matching. The attenuation constant ( $\alpha$ ) was calculated according to the Equation 4 in supplemental information, and the curves of  $\alpha$  varied with  $f$  were shown in Figure S10F. Undoubtedly, S0.7 and S0.9 possess strongest dissipation capacity for EMW, relying on their strong polarization loss coming from defects and heterogeneous interfaces. Comparatively, the declined loss capability of S0.3 and S0.5 is mainly due to the weak lattice defect polarization and interfacial polarization. In summary, the high complex permittivity of  $\text{Fe}_3\text{O}_4$  foams is a double-edged sword, and thereby despite the stronger dielectric loss of S0.7 and S0.9, their EMW absorption performance are still very poor due to the worse impedance matching stemming from the excessive complex permittivity preventing the entrance of EMW. Consequently, considering the prerequisite role of impedance matching in EMW absorption, S0.5, which owns best impedance matching and moderate polarization loss, has the optimum EMW absorbing performance.

The possible EMW absorption mechanism of  $\text{Fe}_3\text{O}_4$  foams is illustrated in Figure 5. In brief, impedance matching, which is affected by the complex permittivity, is the major determinant for EMW absorption performance of  $\text{Fe}_3\text{O}_4$  foams, while microstructure immensely influences the complex permittivity of  $\text{Fe}_3\text{O}_4$  foams. With the raising of CA ratio, the increased complex permittivity, which originates from the increasingly smooth surface and large specific surface area of samples, produce more and more intense polarization loss. Nevertheless, the resultant impedance matching is optimized firstly and worsens lately. Eventually, S0.5 displays the best absorbing performance relying on the optimal impedance matching and moderate polarization loss.

## Conclusion

Lightweight coralloid  $\text{Fe}_3\text{O}_4$  foams shaped by porous curved surface were prepared through a facile sol-gel autocombustion. The complex permittivity can be significantly improved and the density is greatly reduced

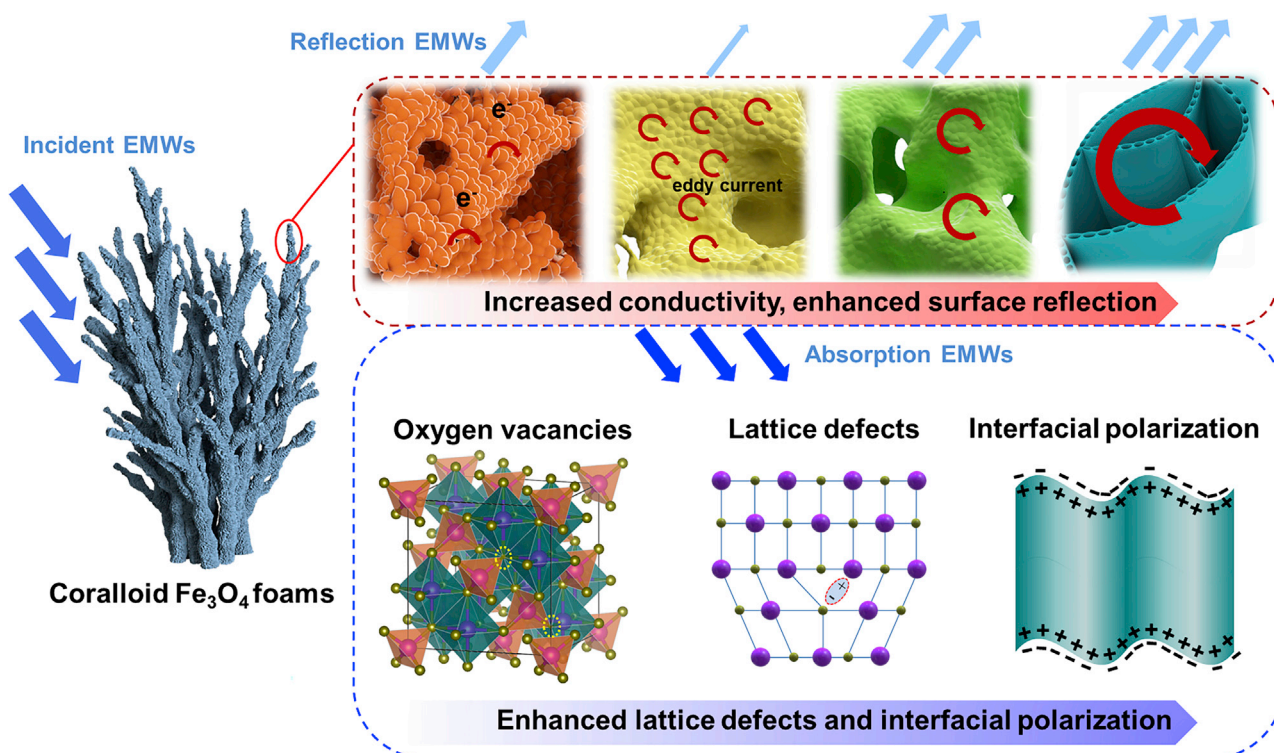


Figure 5. Electromagnetic wave loss mechanism diagram of  $\text{Fe}_3\text{O}_4$  foams

simply by increasing the ratio of citric acid. The proper improvement of complex permittivity can enhance the impedance matching of  $\text{Fe}_3\text{O}_4$  foams, which determines the EMW absorption performance. When the ratio reaches 0.5, the density of  $\text{Fe}_3\text{O}_4$  foams is low to  $0.05078 \text{ g/cm}^3$  and the EAB is up to 6.24 GHz (11.76–18 GHz) at a small thickness of 1.8 mm. Owing to the advantages of light weight and broadband absorption, the as-obtained  $\text{Fe}_3\text{O}_4$  foams have great application potential in the electromagnetic absorption of portable electronic devices, aircraft, and spacecraft.

#### Limitations of the study

Although lightweight and broadband microwave absorbing materials can be obtained through this facile and low-energy method, limited by the sol-gel auto-combustion method itself, the as-obtained  $\text{Fe}_3\text{O}_4$  foam is brittle, which hinders its application in flexible wearable devices. In the follow-up research, it is expected to further expand its application by combining with flexible wave transmitting materials such as polyimide.

#### STAR METHODS

Detailed methods are provided in the online version of this paper and include the following:

- KEY RESOURCES TABLE
- RESOURCE AVAILABILITY
  - Lead contact
  - Materials availability
  - Data and code availability
- METHOD DETAILS
  - Materials
  - Synthesis of  $\text{Fe}_3\text{O}_4$  foams
  - Characterization of  $\text{Fe}_3\text{O}_4$  foams
  - Measurement of electromagnetic parameters
  - Measurement of impedance matching degree and attenuation constant

**SUPPLEMENTAL INFORMATION**

Supplemental information can be found online at <https://doi.org/10.1016/j.isci.2022.103925>.

**ACKNOWLEDGMENTS**

Thanks for the support from the National Natural Science Foundation of China (No. 22004106, 51872238 and 21806129).

**AUTHOR CONTRIBUTIONS**

Q. C. designed research, performed experiments, wrote the manuscript; H. L. analyzed data and drew designs; B. S. analyzed data and reviewed the manuscript; H. W. designed research, instructed the writing and reviewed the manuscript. All authors discussed the results and contributed to the final manuscript.

**DECLARATION OF INTERESTS**

The authors declare no competing interests.

Received: November 22, 2021

Revised: January 10, 2022

Accepted: February 10, 2022

Published: March 18, 2022

**REFERENCES**

- Chang, Q., Liang, H., Shi, B., Li, X., Zhang, Y., Zhang, L., and Wu, H. (2021a). Ethylenediamine-assisted hydrothermal synthesis of  $\text{NiCo}_2\text{O}_4$  absorber with controlled morphology and excellent absorbing performance. *J. Colloid Interf. Sci.* 588, 336–345.
- Chang, Q., Liang, H., Shi, B., and Wu, H. (2021b). Sodium oxalate-induced hydrothermal synthesis of wood-texturecolumn-like  $\text{NiCo}_2\text{O}_4$  with broad bandwidth electromagnetic wave absorption performance. *J. Colloid Interf. Sci.* 600, 49–57.
- Chen, Y., Potschke, P., Pionteck, J., Voit, B., and Qi, H. (2020). Multifunctional cellulose/rGO/ $\text{Fe}_3\text{O}_4$  composite aerogels for electromagnetic interference shielding. *ACS Appl. Mater. Interf.* 12, 22088–22098.
- Cui, X., Liu, W., Gu, W., Liang, X., and Ji, G. (2019). Two-dimensional  $\text{MoS}_2$  modified using  $\text{CoFe}_2\text{O}_4$  nanoparticles with enhanced microwave response in the X and Ku band. *Inorg. Chem. Front.* 6, 590–597.
- Deng, Y., Zheng, Y., Zhang, D., Han, C., Cheng, A., Shen, J., Zeng, G., and Zhang, H. (2020). A novel and facile-to-synthesize three-dimensional honeycomb-like nano- $\text{Fe}_3\text{O}_4@\text{C}$  composite: electromagnetic wave absorption with wide bandwidth. *Carbon* 169, 118–128.
- Fang, Y., Xue, W., Zhao, R., Bao, S., Wang, W., Sun, L., Chen, L., Sun, G., and Chen, B. (2020). Effect of nanoporosity on the electromagnetic wave absorption performance in a biomastemplated  $\text{Fe}_3\text{O}_4/\text{C}$  composite: a small-angle neutron scattering study. *J. Mater. Chem. C* 8, 319–327.
- Gao, S., Zhang, Y., Xing, H., and Li, H. (2020). Controlled reduction synthesis of yolk-shell magnetic@void@C for electromagnetic wave absorption. *Chem. Eng. J.* 387, 124149.
- Guo, S., Wang, L., and Wu, H. (2015). Facile synthesis and enhanced electromagnetic wave absorption of porous  $\text{ZnCo}_2\text{O}_4$  nanosheets. *Adv. Funct. Mater.* 25, 3190–3197.
- Han, R., Li, W., Pan, W., Zhu, M., Zhou, D., and Li, F. (2014). 1D magnetic materials of  $\text{Fe}_3\text{O}_4$  and Fe with high performance of microwave absorption fabricated by electrospinning method. *Sci. Rep.* 4, 14943.
- Han, M., Yin, X., Li, X., Anasori, B., Zhang, L., Cheng, L., and Gogotsi, Y. (2017). Laminated and two-dimensional carbon-supported microwave absorbers derived from MXenes. *ACS Appl. Mater. Interf.* 9, 20038–20045.
- He, N., Yang, X., Shi, L., Yang, X., Lu, Y., Tong, G., and Wu, W. (2020). Chemical conversion of  $\text{Cu}_2\text{O}/\text{PPy}$  core-shell nanowires (CSNWs): a surface/interface adjustment method for high-quality Cu/Fe/C and Cu/ $\text{Fe}_3\text{O}_4/\text{C}$  CSNWs with superior microwave absorption capabilities. *Carbon* 166, 205–217.
- Hua, Z., Deng, Y., Li, K., and Yang, S. (2012). Low-density nanoporous iron foams synthesized by sol-gel autoxidation. *Nano Res. Lett.* 7, 129.
- Huang, C., Zhang, H., Sun, Z., Zhao, Y., Chen, S., Tao, R., and Liu, Z. (2011). Porous  $\text{Fe}_3\text{O}_4$  nanoparticles: synthesis and application in catalyzing epoxidation of styrene. *J. Colloid Interf. Sci.* 364, 298–303.
- Jia, X., Wang, J., Zhu, X., Wang, T., Yang, F., Dong, W., Wang, G., Yang, H., and Wei, F. (2017). Synthesis of lightweight and flexible composite aerogel of mesoporous iron oxide threaded by carbon nanotubes for microwave absorption. *J. Alloy. Compd.* 697, 138–146.
- Jiang, Y., Yang, S., Hua, Z., and Huang, H. (2009). Sol-gel autoxidation synthesis of metals and metal alloys. *Angew. Chem.* 121, 8681–8683.
- Jiang, K., Liu, Y., Pan, Y., Wang, R., Hu, P., He, R., Zhang, L., and Tong, G. (2017). Monodisperse  $\text{NixFe}_{3-x}\text{O}_4$  nanospheres: metal-ion-steered size/composition control mechanism, static magnetic and enhanced microwave absorbing properties. *Appl. Surf. Sci.* 404, 40–48.
- Jin, C., Lu, Y., Tong, G., Che, R., and Xu, H. (2020). Excellent microwave absorbing properties of  $\text{ZnO/ZnFe}_2\text{O}_4/\text{Fe}$  core-shell microrods prepared by a rapid microwave-assisted hydrothermal-chemical vapor decomposition method. *Appl. Surf. Sci.* 531, 147353.
- Jin, L., Wang, J., Wu, F., Yin, Y., and Zhang, B. (2021). MXene@ $\text{Fe}_3\text{O}_4$  microspheres/fibers composite microwave absorbing materials: optimum composition and performance evaluation. *Carbon* 182, 770–780.
- Li, Y., Wu, T., Jiang, K., Tong, G., Jin, K., Qian, N., Zhao, L., and Lv, T. (2016).  $\text{Mn}^{2+}$  induced structure evolution and dual-frequency microwave absorption of  $\text{MnxFe}_{3-x}\text{O}_4$  hollow/porous spherical chains made by one-pot solvothermal approach. *J. Mater. Chem. C* 4, 7119–7129.
- Li, Y., Liu, X., Nie, X., Yang, W., Wang, Y., Yu, R., and Shui, J. (2019a). Multifunctional organic-inorganic hybrid aerogel for self-cleaning, heat-insulating, and highly efficient microwave absorbing material. *Adv. Funct. Mater.* 29, 1807624.
- Li, X., Wang, L., You, W., Xing, L., Yu, X., Li, Y., and Che, R. (2019b). Morphology-controlled synthesis and excellent microwave absorption performance of  $\text{ZnCo}_2\text{O}_4$  nanostructures via a self-assembly process of flake units. *Nanoscale* 11, 2694–2702.
- Li, X., Yin, X., Song, C., Han, M., Xu, H., Duan, W., Cheng, L., and Zhang, L. (2021). Self-assembly core-shell graphene-bridged hollow MXenes spheres 3D foam with ultrahigh specific EM absorption performance. *Adv. Funct. Mater.* 28, 1803938.

Liang, H., Xing, H., Qin, M., and Wu, H. (2020). Bamboo-like short carbon fibers@ $\text{Fe}_3\text{O}_4$ @phenolic resin and honeycomb-like short carbon fibers@ $\text{Fe}_3\text{O}_4$ @ $\text{FeO}$  composites as high-performance electromagnetic wave absorbing materials. *Compos. Part A.* 135, 105959.

Liang, L., Li, Q., Yan, X., Feng, Y., Wang, Y., Zhang, H.B., Zhou, X., Liu, C., Shen, C., and Xie, X. (2021). Multifunctional magnetic  $\text{Ti}_3\text{C}_2\text{T}_x$  MXene/graphene aerogel with superior electromagnetic wave absorption performance. *ACS Nano* 15, 6622–6632.

Liu, Y., Fu, Y., Liu, L., Li, W., Guan, J., and Tong, G. (2018). Low-cost carbothermal reduction preparation of monodisperse  $\text{Fe}_3\text{O}_4$ /C core-shell nanosheets for improved microwave absorption. *ACS Appl. Mater. Interf.* 10, 16511–16520.

Liu, J., Liang, H., and Wu, H. (2020). Hierarchical flower-like  $\text{Fe}_3\text{O}_4/\text{MoS}_2$  composites for selective broadband electromagnetic wave absorption performance. *Compos. Part A.* 130, 105760.

Liu, J., Zhang, L., Zang, D., and Wu, H. (2021a). A competitive reaction strategy toward binary metal sulfides for tailoring electromagnetic wave absorption. *Adv. Funct. Mater.* 31, 2105018.

Liu, P., Gao, S., Zhang, G., Huang, Y., You, W., and Che, R. (2021b). Hollow engineering to Co@N-Doped carbon nanocages via synergistic protecting-etching strategy for ultrahigh microwave absorption. *Adv. Funct. Mater.* 31, 2102812.

Lv, P., Zhao, H., Zeng, Z., Wang, J., Zhang, T., and Li, X. (2014). Facile preparation and electrochemical properties of carbon coated  $\text{Fe}_3\text{O}_4$  as anode material for lithium-ion batteries. *J. Power Sourc.* 259, 92–97.

Lv, H., Yang, Z., Wang, P.L., Ji, G., Song, J., Zheng, L., Zeng, H., and Xu, Z.J. (2018). A voltage-boosting strategy enabling a low-frequency, flexible electromagnetic wave absorption device. *Adv. Mater.* 30, 1706343.

Ma, W., He, P., Wang, T., Xu, J., Liu, X., Zhuang, Q., Cui, Z.K., and Lin, S. (2021). Microwave absorption of carbonization temperature-dependent uniform yolk-shell H- $\text{Fe}_3\text{O}_4$ @C microspheres. *Chem. Eng. J.* 420, 129875.

Meng, X., Yang, W., Han, G., Yu, Y., Ma, S., Liu, W., and Zhang, Z. (2020). Three-dimensional foam-like  $\text{Fe}_3\text{O}_4$ @C core-shell nanocomposites: controllable synthesis and wideband electromagnetic wave absorption properties. *J. Magn. Magn. Mater.* 502, 166518.

Qiao, M., Lei, X., Ma, Y., Tian, L., He, X., Su, K., and Zhang, Q. (2018). Application of yolk-shell  $\text{Fe}_3\text{O}_4$ @N-doped carbon nanochains as highly effective microwave-absorption material. *Nano Res.* 11, 1500–1519.

Qin, M., Zhang, L., and Wu, H. (2020a). Dual-template hydrothermal synthesis of multi-channel porous  $\text{NiCo}_2\text{O}_4$  hollow spheres as high-performance electromagnetic wave absorber. *Appl. Surf. Sci.* 515, 146132.

Qin, M., Lan, D., Wu, G., Qiao, X., and Wu, H. (2020b). Sodium citrate assisted hydrothermal synthesis of nickel cobaltate absorbers with tunable morphology and complex dielectric

parameters toward efficient electromagnetic wave absorption. *Appl. Surf. Sci.* 504, 144480.

Qin, M., Zhang, L., Zhao, X., and Wu, H. (2021a). Lightweight Ni foam-based ultra-broadband electromagnetic wave absorber. *Adv. Funct. Mater.* 31, 2103436.

Qin, M., Zhang, L., Zhao, X., and Wu, H. (2021b). Defect induced polarization loss in multi-shelled spinel hollow spheres for electromagnetic wave absorption application. *Adv. Sci.* 8, 2004640.

Qing, X., Yue, X., Wang, B., and Lu, Y. (2014). Facile synthesis of size-tunable, multilevel nanoporous  $\text{Fe}_3\text{O}_4$  microspheres for application in electromagnetic wave absorption. *J. Alloys Compd.* 595, 131–137.

Shi, Y., Gao, X., and Qiu, J. (2019). Synthesis and strengthened microwave absorption properties of three-dimensional porous  $\text{Fe}_3\text{O}_4$ /graphene composite foam. *Ceramics Int.* 45, 3126–3132.

Sun, G., Dong, B., Cao, M., Wei, B., and Hu, C. (2011). Hierarchical dendrite-like magnetic materials of  $\text{Fe}_3\text{O}_4$ ,  $\gamma\text{-Fe}_2\text{O}_3$ , and Fe with high performance of microwave absorption. *Chem. Mater.* 23, 1587–1593.

Sun, Y., Zhong, W., Wang, Y., Xu, X., Wang, T., Wu, L., and Du, Y. (2017).  $\text{MoS}_2$ -based mixeddimensional van der waals heterostructures: a new platform for excellent and controllable microwave-absorption performance. *ACS Appl. Mater. Interf.* 9, 34243–34255.

Tong, G., Wu, W., Guan, J., Qian, H., Yuan, J., and Li, W. (2011). Synthesis and characterization of nanosized urchin-like  $\alpha\text{-Fe}_2\text{O}_3$  and  $\text{Fe}_3\text{O}_4$ : microwave electromagnetic and absorbing properties. *J. Alloys Compd.* 509, 4320–4326.

Tong, G., Du, F., Xiang, L., Liu, F., Mao, L., and Guan, J. (2014). Generalized green synthesis and formation mechanism of sponge-like ferrite micro-polyhedra with tunable structure and composition. *Nanoscale* 6, 778–787.

Tong, G., Liu, Y., Wu, T., Tong, C., and Du, F. (2015).  $\text{H}_2\text{O}$ -steered size/phase evolution and magnetic properties of large-scale, monodisperse  $\text{Fe}_3\text{O}_4$  nanomaterials. *J. Mater. Chem. C* 3, 5506–5515.

Wang, X., Geng, Q., Shi, G., Xu, G., Yu, J., Guan, Y., Zhang, Y., and Li, D. (2019). One-pot solvothermal synthesis of Fe/ $\text{Fe}_3\text{O}_4$  composites with broadband microwave absorption. *J. Alloys Compd.* 803, 818–825.

Wu, H., Wu, G., Ren, Y., Yang, L., Wang, L., and Li, X. (2015).  $\text{Co}^{2+}/\text{Co}^{3+}$  ratio dependence of electromagnetic wave absorption in hierarchical  $\text{NiCo}_2\text{O}_4\text{-CoNiO}_2$  hybrids. *J. Mater. Chem. C* 3, 7677–7690.

Wu, L., Lu, Y., Shao, W., Wei, H., Tong, G., and Wu, W. (2020). Simple salt-template Assembly for layered heterostructures of C/Ferrite and EG/C/M $\text{Fe}_2\text{O}_4$  (M = Fe, Co, Ni, Zn) nanoparticle arrays toward superior microwave absorption capabilities. *Adv. Mater. Inter.* 7, 2000736.

Wu, Z., Pei, K., Xing, L., Yu, X., You, W., and Che, R. (2019). Enhanced microwave absorption performance from magnetic coupling of magnetic nanoparticles suspended within

hierarchically tubular composite. *Adv. Funct. Mater.* 29, 1901448.

Wei, H., Wang, X., Tong, G., Fan, B., Wang, X., and Wu, W. (2022). Morphology, size, and defect engineering in  $\text{CeOHCO}_3$  hierarchical structures for ultra-wide band microwave absorption. *J. Mater. Chem. C* 10, 281–293.

Wu, H., Liu, J., Liang, H., and Zang, D. (2020a). Sandwich-like  $\text{Fe}_3\text{O}_4/\text{Fe}_3\text{S}_4$  composites for electromagnetic wave absorption. *Chem. Eng. J.* 393, 124743.

Wu, H., Qin, M., and Zhang, L. (2020b).  $\text{NiCo}_2\text{O}_4$  constructed by different dimensions of building blocks with superior electromagnetic wave absorption performance. *Compos. Part A* 182, 107620.

Xiong, Q.Q., Tu, J.P., Lu, Y., Chen, J., Yu, Y.X., Qiao, Y.Q., Wang, X.L., and Gu, C.D. (2012). Synthesis of hierarchical hollow-structured single-crystalline magnetite ( $\text{Fe}_3\text{O}_4$ ) microspheres: the highly powerful storage versus lithium as an anode for lithium ion batteries. *J. Phys. Chem. C* 116, 6495–6502.

Xu, D., Xiong, X., Chen, P., Yu, Q., Chu, H., Yang, S., and Wang, Q. (2019). Superior corrosion-resistant 3D porous magnetic graphene foam-ferrite nanocomposite with tunable electromagnetic wave absorption properties. *J. Magn. Magn. Mater.* 469, 428–436.

Yan, F., Kang, J., Zhang, S., Li, C., Zhu, C., Zhang, X., and Chen, Y. (2018). Enhanced electromagnetic wave absorption induced by void spaces in hollow nanoparticles. *Nanoscale* 10, 18742.

Yang, X., Liu, M., Lan, Y., Wu, L., Ji, R., Tong, G., Gong, P., and Wu, W. (2021).  $\text{Cu}^{2+}$  induced self-assembly of urchin-like  $\text{Co}_{1-x}\text{Cu}_x$  into hollow microspheres toward wideband and thin microwave absorbers. *Chem. Eng. J.* 426, 130779.

Yang, X., Fan, B., Tang, X., Wang, J., Tong, G., Chen, D., and Guan, J. (2022). Interface modulation of chiral PPy/ $\text{Fe}_3\text{O}_4$  planar microhelices to achieve electric/magnetic-coupling and wide-band microwave absorption. *Chem. Eng. J.* 430, 132747.

Zhang, X., Guo, J., Guan, P., Qin, G., and Pennycook, S.J. (2015). Gigahertz dielectric polarization of substitutional single niobium atoms in defective graphitic layers. *Phys. Rev. Lett.* 115, 147601.

Zhang, X., Han, D., Hua, Z., and Yang, S. (2016). Porous  $\text{Fe}_3\text{O}_4$  and gamma- $\text{Fe}_2\text{O}_3$  foams synthesized in air by sol-gel autocombustion. *J. Alloys Compd.* 684, 120–124.

Zhang, C., Chen, Y., Li, H., Tian, R., and Liu, H. (2018). Facile fabrication of three-dimensional lightweight RGO/PPy nanotube/ $\text{Fe}_3\text{O}_4$  aerogel with excellent electromagnetic wave absorption properties. *ACS Omega* 3, 5735–5743.

Zhang, M., Jiang, Z., Lv, X., Zhang, X., Zhang, Y., Zhang, J., Zhang, L., and Gong, C. (2020). Microwave absorption performance of reduced graphene oxide with negative imaginary permeability. *J. Phys. D Appl. Phys.* 53, 02LT01.

Zhang, H., Cheng, J., Wang, H., Huang, Z., Zheng, Q., Zheng, G., Zhang, D., Che, R., and Cao, M. (2021). Initiating VB-Group laminated  $\text{NbS}_2$  electromagnetic wave absorber toward superior absorption bandwidth as large as 6.48 GHz through phase engineering modulation. *Adv. Funct. Mater.* 32, 2108194.

Zhao, Z., Zhou, X., Kou, K., and Wu, H. (2020a). PVP-assisted transformation of ZIF-67 into cobalt layered double hydroxide/carbon fiber as electromagnetic wave absorber. *Carbon* 173, 80–90.

Zhao, B., Li, Y., Zeng, Q., Wang, L., Ding, J., Zhang, R., and Che, R. (2020b). Galvanic replacement reaction involving core-shell magnetic chains and orientation-tunable microwave absorption properties. *Small* 16, e2003502.

Zhao, B., Bai, P., Wang, S., Ji, H., Fan, B., Zhang, R., and Che, R. (2021). High-performance Joule heating and electromagnetic shielding properties of anisotropic carbon scaffolds. *ACS Appl. Mater. Inter.* 13, 29101–29112.

Zhou, X., Zhang, C., Zhang, M., Feng, A., Qu, S., Zhang, Y., Liu, X., Jia, Z., and Wu, G. (2019). Synthesis of  $\text{Fe}_3\text{O}_4$ /carbon foams composites with broadened bandwidth and excellent electromagnetic wave absorption performance. *Compos. Part A*, 127, 105627.

Zhou, W., Jiang, C., Duan, X., Song, J., Yuan, Y., and Chen, N. (2020).  $\text{Fe}_3\text{O}_4$ /carbonized cellulose micro-nano hybrid for high-performance microwave absorber. *Carbohyd. Polym.* 245, 116531.

## STAR★METHODS

### KEY RESOURCES TABLE

REAGENT or RESOURCE	SOURCE	IDENTIFIER
<b>Chemicals</b>		
Iron(III) nitrate nonahydrate (AR, 98.5%)	Macklin	CAS:7782-61-8
Citric acid monohydrate (AR, 99.5%)	Macklin	CAS:5949-29-1
Ammonium hydroxide solution (AR, 25-28%)	Macklin	CAS:1336-21-6
<b>Deposited data</b>		
All data reported in this paper will be shared by the lead contact upon request.		

### RESOURCE AVAILABILITY

#### Lead contact

Further information and requests for resources and reagents should be directed to and will be fulfilled by the lead contact, Hongjing Wu ([wuhongjing@nwpu.edu.cn](mailto:wuhongjing@nwpu.edu.cn)).

#### Materials availability

This study did not generate new unique reagents.

#### Data and code availability

All data reported in this paper will be shared by the lead contact upon request. This paper does not report original code. Any additional information required to reanalyze the data reported in this paper is available from the lead contact upon request.

### METHOD DETAILS

#### Materials

Iron (III) nitrate nonahydrate ( $\text{Fe}(\text{NO}_3)_3 \cdot 9\text{H}_2\text{O}$ , 98.5%), Citric acid monohydrate (CA, 99.5%) and Ammonium hydroxide solution (25-28%) were procured from Macklin. All regents used in this work are analytical grade and applied directly without further purification.

#### Synthesis of $\text{Fe}_3\text{O}_4$ foams

The preparation process of  $\text{Fe}_3\text{O}_4$  foams referenced the previous studies (Zhang et al., 2016; Jiang et al., 2009) and made some adjustments. In a typical protocol, 10 mmol iron (III) nitrate nonahydrate ( $\text{Fe}(\text{NO}_3)_3 \cdot 9\text{H}_2\text{O}$ ) and a certain amount of citric acid (CA) monohydrate ( $\text{C}_6\text{H}_8\text{O}_7 \cdot \text{H}_2\text{O}$ ) were first dissolved in 50 mL distilled water and stirred for 10 min. Secondly, ammonia was added dropwise to the above mixed solution under continuous stirring until the pH value reached 7, keeping stirring for 30 min to obtain a transparent sol. Thirdly, the sol was placed in an oven designated at 95°C and dried for 24 hours to form a dry gel, and then, the dry gel was ignited in a muffle furnace preheated at 200°C and annealed for 1 hour, through which the gel was burned by self-propagating combustion and formed loose coraloid  $\text{Fe}_3\text{O}_4$  foams. The mole ratio of CA to ferric nitrate is set as 0.1, 0.3, 0.5, 0.7 and 0.9 to investigate the variation of electromagnetic parameters on proportion, and the corresponding products were signed as S0.1, S0.3, S0.5, S0.7, S0.9, respectively. See in Figure S1 for photos of products at different stages of the synthesis process.

#### Characterization of $\text{Fe}_3\text{O}_4$ foams

The crystalline structure and phase composition of samples were analyzed by X-ray diffractometer (XRD, with  $\text{Cu K}\alpha$  radiation) in the angular range of 10-90° and Raman Spectroscopy (Raman, WITec Alpha300R) in wavenumber of 50-700  $\text{cm}^{-1}$ , respectively. The element valence analysis was carried out through X-ray photoelectron spectroscopy (XPS, Kratos Axis Supra). The morphologies and microstructures were observed by emission scanning electron microscope (FESEM, JSM-7610F) and high-resolution

transmission electron microscope (HRTEM, FEI Tecnai G2 F20 STWIN). N<sub>2</sub> adsorption-desorption isothermometer (Micromeritics, ASAP2020) was conducted to investigate the pore characteristics of products. The specific surface areas ( $S_{BET}$ ) were calculated by Brunauer-Emmett-Teller (BET) method using adsorption data in a relative pressure ranged from 0.000032 to 0.99 and the pore volumes and pore size distributions were derived from the nitrogen isotherms by the Barrett-Joyner-Halenda (BJH) method. The conductivity of samples was studied by electrochemical impedance spectroscopy (EIS, CHI660E) in the frequency range of 0.1 to  $1 \times 10^5$  Hz with amplitude of 5 mV. The magnetic properties were measured by magnetic measurement system (Quantum Design, MPMS3) at room temperature. Volume measurement was carried out for Fe<sub>3</sub>O<sub>4</sub> samples: in terms of lamellar Fe<sub>3</sub>O<sub>4</sub> (S0.3), the flake was cut into square (1cm × 1cm) and measured thickness to obtain the volume. As for coralloid Fe<sub>3</sub>O<sub>4</sub> samples (S0.5, S0.7 and S0.9), the samples were cut into small section with a length about 5 mm; then transferred to a measuring cylinder and compressed tightly without destroying the structure to measure the volume. Finally, density is obtained by dividing mass by volume.

### Measurement of electromagnetic parameters

The electromagnetic parameters measurement was carried out by a vector network analyzer (Anritsu MS46322B) in a frequency range of 2-18 GHz. Firstly, the as-prepared Fe<sub>3</sub>O<sub>4</sub> samples were mixed with paraffin wax at a mass ratio of 7:3, and then the mixture was pressed into a toroid shape ( $\varphi_{in} = 3.04$  mm,  $\varphi_{out} = 7.00$  mm) for test. The reflection loss (RL) of the samples was calculated based on the transmission line theory (Chang et al., 2021a), and the formulas were listed below:

$$RL = 20 \log \left| \frac{Z_{in} - Z_0}{Z_{in} + Z_0} \right| \quad (\text{Equation 2})$$

$$Z_{in} = Z_0 \sqrt{\frac{\mu_r}{\epsilon_r}} \tanh \left( j \frac{2\pi f d}{c} \sqrt{\mu_r \epsilon_r} \right) \quad (\text{Equation 3})$$

where  $\epsilon_r$  represents relative complex permittivity ( $\epsilon_r = \epsilon' - j\epsilon''$ ),  $\mu_r$  is relative complex permeability ( $\mu_r = \mu' - j\mu''$ ),  $Z_{in}$  represents the input impedance of absorbent,  $Z_0$  is intrinsic impedance in air,  $f$  represents EMW frequency,  $d$  is the thickness of absorbent, and  $c$  is the velocity of light in vacuum.

### Measurement of impedance matching degree and attenuation constant

The impedance matching degree can be evaluated through the formula:

$$|\Delta| = \left| \sinh^2(Kfd) - M \right| \quad (\text{Equation 4})$$

where the values of  $K$  and  $M$  can be expressed as:

$$K = \frac{4\pi\sqrt{\mu'\epsilon'} \times \sin(\frac{\delta_e + \delta_m}{2})}{c \times \cos\delta_e \times \cos\delta_m} \quad (\text{Equation 5})$$

$$M = \frac{4\mu'\cos\delta_e \times \epsilon' \times \cos\delta_m}{(\mu'\cos\delta_e - \epsilon'\cos\delta_m)^2 + \left[ \tan\left(\frac{\delta_m - \delta_e}{2}\right) \right]^2 (\mu'\cos\delta_e + \epsilon'\cos\delta_m)^2} \quad (\text{Equation 6})$$

The attenuation constant ( $\alpha$ ) was calculated according to the equation below:

$$\alpha = \frac{\sqrt{2\pi f}}{c} \times \sqrt{(\mu''\epsilon'' - \mu'\epsilon') + \sqrt{(\mu''\epsilon'' - \mu'\epsilon')^2 + (\mu'\epsilon'' + \mu''\epsilon')^2}} \quad (\text{Equation 7})$$